Nuclear Materials and Energy 24 (2020) 100759

Contents lists available at ScienceDirect

Nuclear Materials and Energy

journal homepage: www.elsevier.com/locate/nme

Relationships between depth-resolved primary radiation damage, irradiation-induced nanostructure and nanoindentation response of ion-irradiated Fe-Cr and ODS Fe-Cr alloys

K. Vogel, C. Heintze, P. Chekhonin, S. Akhmadaliev, E. Altstadt, F. Bergner*

Helmholtz-Zentrum Dresden-Rossendorf, Bautzner Landstr. 400, 01328 Dresden, Germany

ARTICLE INFO

Keywords:
Fe-alloys
Ion irradiation
TEM
Nanoindentation
Irradiation hardening

ABSTRACT

Ion irradiations are indispensable for exploring radiation effects on materials, for example, radiation hardening. However, the extraction of radiation hardening as function of displacement damage from the nanoindentation (NI) response of self-ion-irradiated metallic alloys is a challenge. In particular, recent attempts suffer from interference with contributions arising from injected self-interstitial atoms. Moreover, instances of available microstructural evidence and NI results reported for the same material and same irradiation are rare. In order to tackle these issues, the depth-dependent irradiated microstructure and the NI response were analyzed for Fe-9Cr and oxide dispersion strengthened Fe-Cr alloys irradiated with 5 MeV iron ions. Cross-sectional transmission electron microscopy indicated the appearance of irradiation-induced dislocation loops but no other types of visible microstructural changes. NI indicated maxima of the radiation hardening as function of contact depth. Links between the depth-resolved primary radiation damage, the observed depth-dependent characteristics of loops and the measured hardening are considered. As a key point, the link between loops and hardening requires the integration of the local hardening contributions over the indentation plastic zone. Calculations and measurements are compared with respect to both the depth position of maximum hardening and the substrate effect. The role of the model assumptions is discussed with special emphasis on the plastic zone size and the superposition of hardening contributions. The latter is found to be material-specific. The model also allows hardening contributions arising from displacement damage and injected interstitials to be separated.

1. Introduction

Irradiation of metallic materials with MeV ions gives rise to several effects including (i) the displacement of atoms from their lattice sites, mainly in the form of displacement cascades, (ii) the deposition of the injected ions in the metal lattice, (iii) the formation and evolution of irradiation-induced defect clusters such as dislocation loops, and (iv) hardening as consequence of (i) to (iii). Each of these processes is strongly dependent on the distance from the irradiated surface. One of the long-term objectives of ion irradiation is to extract hardening as a function of displacement damage. In the present experimental study, the effect of 5 MeV Fe-ion irradiation of Fe-based materials on microstructure and hardening is addressed. As a rule of thumb, 5 MeV Fe ions modify Fe-based materials in a depth range up to approximately 2 μm.

Processes related to (i) and (ii) can be simulated using the binary collision code SRIM [1,2]. This code is capable of estimating the depth profiles of both the displacement damage in units of displacements per atom (dpa) and the injected self-interstitials per atom (ipa). While more detailed descriptions of primary radiation damage have recently become available [3,4], the present work is restricted to the use of SRIM calculations for the sake of comparability with reported work.

The long-term evolution of dislocation loops or other ion-irradiation-induced defect/solute clusters (iii) in engineering materials, besides being depth-dependent, may strongly depend on both the initial microstructure and the irradiation conditions. Cross-sectional transmission electron microscopy (TEM) was frequently used to qualitatively characterize the depth-dependent distribution of irradiation-induced dislocation loops in particular cases, e.g. [5,6] for pure Fe, [7] for Fe-9%Cr, [8,9] for oxide dispersion strengthened (ODS) steels, [10] for austenitic stainless steels, and [11] for a ferritic/martensitic steel. Quantitative characteristics of the loop distribution as function of depth were reported in some studies, e.g. [5,9,10]. Other nanofeatures that may form as a result of ion irradiation in particular cases include Cr-rich α′-phase particles [12] and Ni-Si-P-Cr-enriched clusters [13].

* Corresponding author.
E-mail address: f.bergner@hzdr.de (F. Bergner).

https://doi.org/10.1016/j.nme.2020.100759
Received 5 February 2020; Received in revised form 27 April 2020; Accepted 29 May 2020
Available online 05 June 2020
2352-1791/ © 2020 The Author(s). Published by Elsevier Ltd. This is an open access article under the CC BY license (http://creativecommons.org/licenses/by/4.0/).

Moreover, ion-irradiation to high doses may give rise to changes of the size distribution of oxide nanoparticles in ODS alloys, see [14] for a recent review. While the present study is focussed on the TEM-visible dislocation loops, other possible contributions will be addressed in the discussion section.

The characterization of ion-irradiated metals with respect to irradiation hardening (iv) as function of indentation depth has become popular as a result of the availability of commercial nanoindentation (NI) devices. Issues with this approach were discussed by Hosemann et al. [15]. For studies on ion-irradiation-induced hardening of Fe-based alloys, we refer to [16–27], for a recent review, see [28]. Two aspects are of particular relevance: First, NI is an integrating method, integration being performed over the indentation plastic zone. For ion-irradiated materials, the volume assumed by the plastic zone typically exhibits steep damage gradients. To gain information on the irradiation response, the depth of the plastic zone should ideally coincide with the thickness of the irradiated layer. Assuming a generally accepted ratio between plastic zone size and indentation depth between 5 and 10, the analyzed range of indentation depth should cover the range from less than 10% to more than 20% of the thickness of the irradiated layer. The shape of the plastic zone is an issue. While most reported studies are based on the half-sphere approximation, e.g. [24,25,29,30], few studies considered deviations from a half-sphere shape [20,22,31]. The problem is that the shape of the plastic zone depends on the depth-dependent hardness [30] and, simultaneously, the latter depends on the former. Second, the depth-dependent hardening is superimposed with the well-known indentation size effect (ISE) [29,32–35]. While hardening mechanisms operating in uniform deformation are well understood, e.g. [36–40], the extraction of the actual depth-dependent local hardness/hardening from NI experiments [19,22–25] is still a challenge and requires experimental verification in addition to just successful fitting. It is important to note that the effect of the injected self-interstitials was not explicitly addressed in the reported NI studies.

The superposition rule of hardening contributions has been a key issue over decades [36,39,41–44]. Most of the suggested rules [36,42] (but not all [43]) are between linear and square superposition. Some recent studies related especially to NI of ion-irradiated samples made use of linear superposition of hardness contributions arising from pre-existing and ion-irradiation-induced barriers [24,25,31]. These authors also averaged the depth-dependent hardness, as opposed to the square of hardness, over the plastic zone. Direct experimental evidence on the irradiation-induced microstructure of the investigated samples was not exploited in these studies. Instead, a power law relationship between hardness and displacement damage [45,46] was assumed, but both the pre-exponential factor and the exponent may strongly vary as functions of the material, microstructure and irradiation conditions [31]. The conclusion is that direct microstructural evidence on the hardening features is required. In another recent study [9], linear superposition of pre-existing and irradiation-induced barriers was combined with averaging of the dislocation line length over the plastic zone, the latter corresponding to averaging the square of hardness instead of the hardness itself. Noteworthy, experimental evidence on the irradiation-induced microstructure was included in [10]. However, the authors of the latter study only reported indentation hardness for a single indentation depth, meaning that the full depth dependence of hardness was not available for verifying the assumptions. Arguments, specific for the case of ion irradiation, in favour of square superposition of pre-existing and irradiation-induced barriers in combination with averaging the square of hardness were also reported [23,26]. These authors achieved reasonable fitting of the model with reported NI data, but did not provide own experimental evidence on the irradiation-induced microstructures in support of the model. Consequently, the type of superposition/averaging has to be considered as case-specific.

In the present study, results on the irradiation-induced microstructure and the NI response are reported for an ion-irradiated Fe-8.4 wt%Cr model alloy (denoted Fe-9Cr) and an ODS Fe-9.1 wt%Cr alloy (denoted ODS FeCr) of different initial microstructure and intentionally different initial hardness. In the discussion section, the link between the depth profiles of displacement damage, injected interstitials, and number density of irradiation-induced loops is addressed first. The second and major part of the discussion, Section 4.2, is dedicated to the microstructure-informed "prediction" of the hardening as function of contact depth, which requires assumptions be made. Here we apply the half-sphere approximation of the indentation plastic zone [24,25,29,30,32] and the dispersed barrier hardening (DBH) model [37,47] including variations of the plastic zone size and the type of superposition of individual hardening contributions. The appropriateness of the resulting "predictions" and underlying assumptions is assessed one by one by way of comparison with the most striking features of the measured hardening as functions of the indentation contact depth. In Section 4.3, the total "predicted" hardening is decomposed, apparently for the first time, into a contribution caused solely by displacement damage and a contribution caused solely by the injected interstitials. Section 4.4 is dedicated to evidence on the absence or possible presence of hardening features in addition to dislocation loops. Taking into account this insight, the applied superposition rules are reconsidered in Section 4.5.

2. Experiments

2.1. Materials

The materials investigated in this study are a commercial-purity Fe-Cr model alloy (8.4 wt% Cr) and an ODS Fe-Cr (9.1 wt% Cr) alloy of different initial microstructure and intentionally different initial hardness.

The Fe-Cr model alloy, here referred to as Fe-9Cr, was produced at Ghent University (Belgium) [48]. The ingots were cold worked under protective atmosphere to produce 9 mm thick plates. The plates were heat-treated at 1050 °C for 3 h in high vacuum for austenitization followed by air cooling. Tempering was performed at 730 °C for 4 h. The composition is given in Table 1. An inverse pole figure (IPF) map obtained by electron backscatter diffraction (EBSD) is shown in Fig. 1. The microstructure consists of tempered martensite with minor contributions of ferrite.

The ODS Fe-Cr-based alloy was supplied by CEA Saclay (France) [49]. Gas-atomized powder was blended with 0.25 wt% Y_2O_3 and milled in a vertical attritor under hydrogen atmosphere protection. Encapsulation, degassing, hot extrusion and air cooling were performed to produce extruded bars. The material was investigated in the as-received condition. Composition and an EBSD IPF-Z map are shown in Table 1 and Fig. 1, respectively. The material exhibits a ferritic microstructure. Basic microstructural parameters and yield stress of both materials are listed in Table 2.

Samples of 10 × 10 × 1 mm^3 were prepared before ion irradiation. The samples were mechanically polished with automatic grinding up to 2500 grit. After mechanically polishing with diamond suspension they were electrolytically polished in solution of 2% perchloric acid in 98% ethylene glycol monobutyl ether for about 3 min to remove the surface damage introduced by mechanical polishing. The procedure was checked by means of depth-resolved positron annihilation spectroscopy [51] for a similar material. The arithmetical mean roughness value R_a of the electro-polished surface was found to be 0.017 μm for Fe-9Cr.

Table 1
Composition in wt% [48,49].

Material	Code	C	Mn	Si	Ti	Cr	Ni	Y_2O_3
Fe-9Cr	L252	0.02	0.03	0.09	0.003	8.4	0.07	–
ODS FeCr	L22-M1	0.1	0.3	0.3	0.3	9.1	0.2	0.25

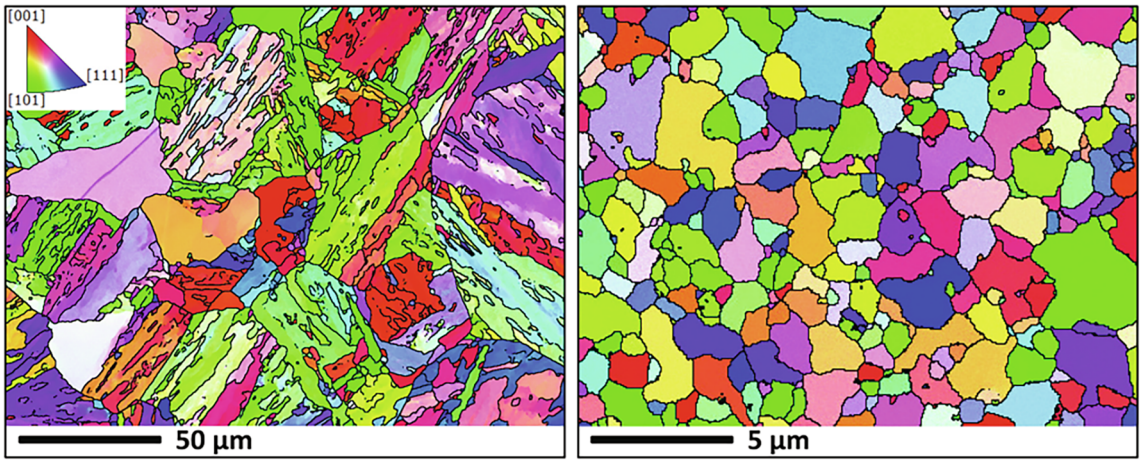

Fig. 1. EBSD IPF-Z maps for Fe-9Cr (left) and ODS FeCr (right).

Table 2
Microstructure parameters and yield stress [49].

Property	Fe-9Cr	ODS FeCr
Grain size (µm)	3 (47*)	1.2
Dislocation density (m^{-2})	0.6×10^{14}	0.5×10^{14}
Number density of oxide particles (m^{-3})	–	1×10^{23}
Mean size of oxide particles (nm)	–	4
Yield stress (MPa)	289	720

* Prior austenite grain size [50].

2.2. Ion irradiation

Ion irradiations were performed with the 3 MV tandetron accelerator of the Ion Beam Center at HZDR Dresden. Fe^{2+} ions of 5 MeV energy were implanted into the polished sides of the samples. The irradiation temperature of 300 °C was maintained by fixing the samples on a heating target. The temperature control was based on a thermocouple placed on the backside of one sample. The samples were scanned by a properly focussed ion beam such that the irradiated area received a laterally uniform exposure corresponding to the respective predetermined target values. The frequency of scanning was approximately 1 kHz. The ion flux was monitored continuously by means of Faraday cups and integrated to obtain the ion fluence. The average ion flux is summarized in Table 3 along with other irradiation parameters. The profiles of displacement damage in units of displacements per atom (dpa) and injected interstitials per atom (ipa) were calculated using the SRIM-2013.00 binary collision code according to the recommendations in [2] using the quick Kinchin-Pease calculation and a displacement energy of 40 eV. The respective profiles are plotted in Fig. 2 [52].

2.3. TEM study of irradiation-induced defects

Cross-sectional TEM samples of the irradiated material were prepared by focused ion beam (FIB) technique using a Zeiss NVision 40 instrument. The microstructure was studied in a FEI Talos F200X transmission electron microscope operated at 200 kV. Irradiation-induced dislocation loops were imaged under various diffraction

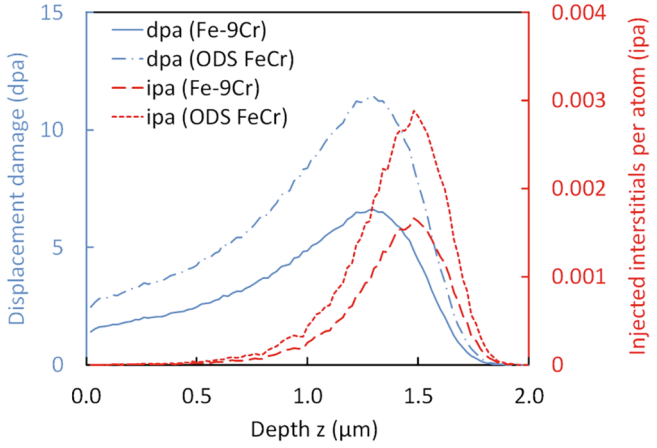

Fig. 2. Depth profiles of displacement damage (dpa) and injected interstitials per atom (ipa) resulting from the performed ion irradiations of Fe-9Cr and ODS FeCr.

conditions in bright- and dark-field conventional TEM mode and, in case of the Fe-9Cr model alloy, additionally with bright- and annular dark-field STEM mode. The number densities of loops were counted in images taken with the diffraction vector $\mathbf{g} = \langle 1\ 1\ 0 \rangle$. The depth profiles of the loop number density and size were obtained by defining and analyzing segments of 100 nm thickness in the direction perpendicular to the surface. The thicknesses of the lamellae were estimated by means of convergent beam electron diffraction. The number density N_c of counted loops with $\mathbf{g} = \langle 1\ 1\ 0 \rangle$ has to be corrected to account for the invisibility of loops with $\mathbf{g}\cdot\mathbf{b} = 0$. Taking into account that only loops with Burgers vectors $\mathbf{b} = a\langle 1\ 0\ 0 \rangle$ and $\mathbf{b} = \frac{1}{2} a\langle 1\ 1\ 1 \rangle$ (a is the lattice constant) form in body-centred cubic Fe-based alloys, the total number density of loops N lies between $1.5N_c$ and $2N_c$ [50]. Therefore, it is reasonable to assume $N \approx 1.75N_c$ with an error range of 1.75 ± 0.25. This relationship was applied for ODS FeCr, for which it was not reasonably possible to specify the fractions of $\langle 1\ 0\ 0 \rangle$- and $\frac{1}{2}\langle 1\ 1\ 1 \rangle$-type loops because of the smallness of the loops. For Fe-9Cr, the ratio of the number densities of loops with $\mathbf{b} = a\langle 1\ 0\ 0 \rangle$ and

Table 3
Summary of irradiation conditions.

Material	Average ion flux (10^{11} cm^{-2} s^{-1})	Average damage rate* (10^{-5} dpa/s)	Total irradiation time	Total displacement damage*
Fe-9Cr	1.6	6	11.6 h	2.5 dpa
ODS FeCr	1.4	5.2	23.1 h	4.3 dpa

* At 500 nm depth.

b = ½ *a*⟨1 1 1⟩ was determined according to [53] using images recorded with **g** = ⟨1 1 0⟩ and **g** = ⟨2 0 0⟩ taken in the depth range from 400 to 650 nm. The result corresponds to $N \approx 1.68N_c$, which is assumed to be representative for the whole depth range. The loop diameter was measured along the largest dimension of bright-field images of the loops. In the present approach, we did not discriminate between vacancy-type and interstitial-type loops.

In order to check the size distribution of oxide nanoparticles in ODS FeCr with respect to both spatial variations and irradiation-induced changes, the TEM imaging conditions were selected such as to minimize the diffraction contrast of loops. Standard image processing using the program ImageJ, including contrast enhancement and conversion to black and white, was used to improve the contrast between particles and matrix.

For both materials, the TEM-analysed region extended over several grains or martensite laths. Therefore, adjustments of the diffraction conditions had to be made for each grain considered for counting and sizing to obtain similar contrast. In order to check for representativeness of the results obtained from the FIB lamella and to evaluate potential contributions related to FIB-induced damage, a plan view sample (TEM foil parallel to the irradiated surface) was extracted from a depth of about 500 nm for the Fe-9Cr model alloy using the electrolytic thinning following the method described in [50].

2.4. Nanoindentation

Nanoindentation hardness H_{IT} was measured at room temperature using a Universal Nanomechanical Tester (UNAT, ASMEC GmbH, now with Zwick-Roell GmbH) equipped with a Berkovich indenter. The area function of the indenter has been calibrated by means of fused silica and sapphire with known bulk moduli. The quasi continuous stiffness measurement mode was applied in order to determine the contact stiffness and calculate the contact depth according to the Oliver-Pharr method [54,55]. Load control was applied with measurements of the contact stiffness automatically conducted at 75 equidistant loads. The maximum loads were 50 mN and 100 mN for Fe-9Cr and ODS FeCr, respectively. The hardness-versus-depth plots were calculated from about 30 indentation tests by averaging after manually excluding, based on the quality of automatic surface detection, occasional corrupted tests. The NI device is suitable for indentation depths larger than approximately 100 nm. For smaller depths, measurements are formally possible but errors increase rapidly under the present conditions. Results at depths smaller than 100 nm have been ignored in the analysis. As a depth of 100 nm corresponds to approximately 5% of the thickness of the irradiated layer, a sufficient number of NI data points with plastic zones fully enclosed in the irradiated layer is available.

3. Results

3.1. TEM study of irradiation-induced defects

For both materials, irradiation-induced dislocation loops were observed as the one and only type of irradiation-induced TEM-visible defects. A loop-rich band was found to form in a certain depth range below the irradiated surface. Fig. 3a displays a TEM bright-field image of the FIB lamella of ODS FeCr, where the defect-rich band, aligned parallel to the specimen surface, is visible in the depth range from 1.2 to 1.6 μm. The band contains a large number of dislocation loops appearing as black dots under two-beam kinematical bright-field conditions and as white dots under weak-beam dark-field conditions, as demonstrated in Fig. 3b and c, respectively. Loops are also visible in the area above the band, but not in the unirradiated substrate. In order to distinguish irradiation-induced loops from pre-existing nm-size ODS particles, an additional image from the same area was acquired with the diffraction contrast minimized, Fig. 3d.

Fig. 4 shows a representative STEM BF micrograph of the cross-section of the ion-irradiated layer in the Fe-9Cr model alloy taken with **g** = [0$\bar{1}$1] close to the [011] zone axis. The upper edge of the image coincides with the sample surface. As in the previous case, a clearly discernible defect-rich band parallel to the surface is observed close to the lower edge of the image. Contrary to ODS FeCr, some of the dislocation loops appear to be arranged along the ⟨0$\bar{1}$1⟩ direction in images taken close to the ⟨011⟩ zone axis, especially from about 650 nm to 1 μm depth. However, a random distribution of loops is observed for images taken close to the ⟨$\bar{1}$11⟩ zone axis. This is consistent with a 2-dimensional distribution of loops on {100} planes as reported by Gao et al. [6]. Zones denuded of dislocation loops of about 50 nm width are observed along grain boundaries. The observations made in the plan view sample confirm the presence of denuded zones along grain boundaries. Some indications of loop arrangements similar to those observed in the FIB lamella were found mainly in thicker regions of the plan view sample. The number densities as well as the size distribution of loops measured in the plan view sample agree well with the results obtained for a depth of 500 nm in the FIB lamella. The latter indicates that FIB artefacts affecting the results in terms of number densities and sizes of loops can be excluded.

The loops were counted and sized segment by segment as described in Section 2.3. For each segment, the counted number of loops was used to calculate the number density N_c. The results are shown in Fig. 5. The depth dependence of N_c (solid blue lines) was parameterized, for the purpose of adjustment and interpolation, using a straight line, a third degree polynomial and a constant value of zero for the depth ranges indicated by the dashed black lines. In Fig. 5b, the data points obtained for Grains 1 and 2 (see Fig. 3a) are highlighted. For Fe-9Cr, the derived depth dependence of the loop diameter is displayed in the inset of Fig. 5a. For ODS FeCr, the loop sizes are close to the detection limit. We have found that $d = 4$ nm is representative for the whole depth range with reasonable accuracy.

Image processing of TEM micrographs, such as the one shown in Fig. 3d, was used in order to enhance the visibility of oxide nanoparticles in ODS FeCr. The same image processing parameters, in particular contrast enhancement and black-white threshold, were applied to the micrographs representing the unirradiated and the irradiated condition. The black-and-white contrast, black areas representing oxide nanoparticles, is shown in Fig. 6 for the unirradiated (Fig. 6a) and ion-irradiated (Fig. 6b) areas of a FIB TEM sample. The positions are marked in Fig. 3a. We have found insignificant, if any, differences between the unirradiated and irradiated areas with respect to both mean size and number density of particles. In any case, possible minor differences are smaller than the observed spatial heterogeneity of the particle distribution as represented, for example, by the upper versus lower half of the image for the unirradiated material in Fig. 6a or the left versus right half of the irradiated material in Fig. 6b. Hence, it can be assumed in the further analysis that the oxide nanoparticles do not give rise to noticeable irradiation-induced hardness differences.

3.2. Microstructure as function of primary radiation damage

The goal of this section is to express the total number density of loops N (in units of 10^{-5} nm^{-3}) as a function of both displacement damage D in units of dpa and injected interstitial atoms E in units of ipa. N, D, and E are functions of the distance z from the irradiated surface. There are good reasons to assume a relationship of the form:

$$N(z) = a_1[D(z)]^p + a_2E(z) \quad (1)$$

Indeed, a power-law dependence of N on D, in a limited range of displacement damage, is consistent with a power-law dependence of

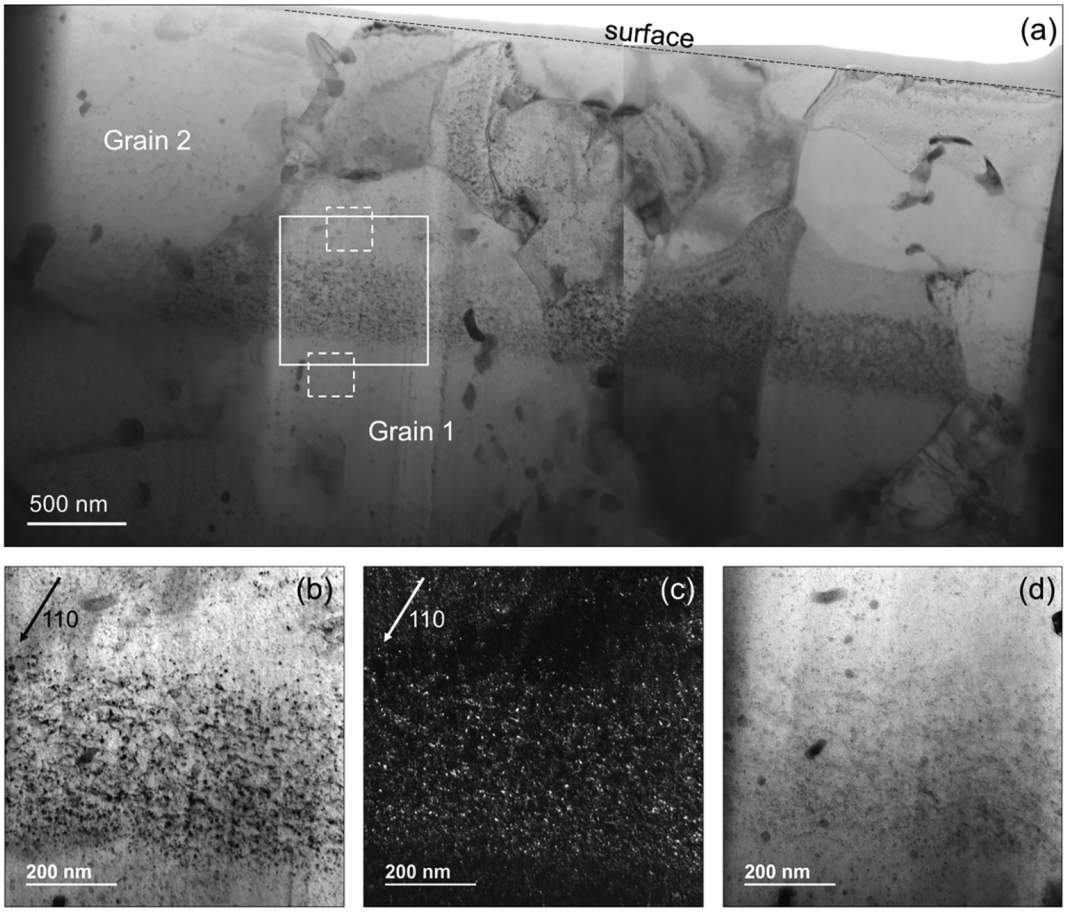

Fig. 3. TEM images of ion-irradiated ODS FeCr. (a) Overview, (b) two-beam kinematical bright-field, (c) weak-beam dark-field, and (d) bright-field image (diffraction contrast minimized) of the area marked with a solid line in (a). The small dashed-line squares in (a) mark areas used for the characterization of oxide nanoparticles.

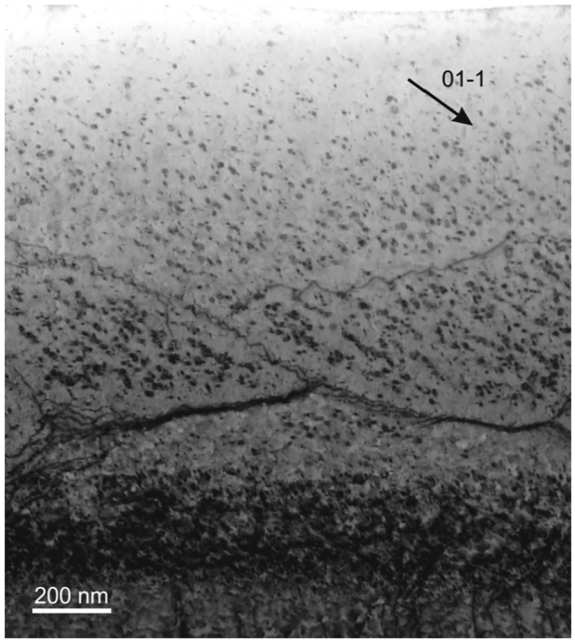

Fig. 4. Overview STEM BF image of the ion-irradiated Fe-9Cr model alloy acquired in two-beam condition with $\mathbf{g} = [0\bar{1}1]$ close to the [011] zone axis.

hardening as function of the displacement damage D, as reported for neutron-irradiated materials [45,46] (for which there are no injected interstitials). It is also reasonable to assume that a depth-independent fraction of the injected interstitials ends up in loops, while the majority of injected interstitials annihilates with vacancies or gets lost in point defect sinks. That means, the injected interstitials add a number density of loops proportional to $E(z)$. The experimental values of $N(z)$ were derived from the counted loops N_c shown in Fig. 5 (solid lines) taking into account the factors 1.68 and 1.75 for Fe-9Cr and ODS FeCr, respectively, in order to correct for invisible loops, see Section 2.3 for the explanation of the choice of these factors. Units of 10^{-5} nm^{-3} = 10^{22} m^{-3} are used for $N(z)$. $D(z)$ and $E(z)$ were taken from Fig. 2 in units of dpa and ipa (interstitials per atom). The effects of D and E were treated as mutually independent as a first approximation. Instead of applying a least-squares procedure with the need to handle z-dependent weights, we found a heuristic approach more robust. The idea was to find combinations of the parameters a_1, p ($0 < p < 1$), and a_2 that meet the following targets:

- to provide a good fit of $N(z)$ in the range of small z, where the concentration of injected interstitials E is close to zero and can be neglected,
- to reflect the maximum of $N(z)$ well,
- to reproduce the z position of the peak of $N(z)$ well.

The fits according to Eq. (1) are shown in Fig. 7. The best values of the parameters given in Table 4 represent trade-offs between the three targets. For Fe-9Cr, the initial slope, the height, and the position of the peak are well represented, but it was impossible to match the width of the peak based on Eq. (1). For ODS FeCr, the height of the peak is well represented and a reasonable compromise between initial slope and depth position of the peak was reached, but it was impossible to match

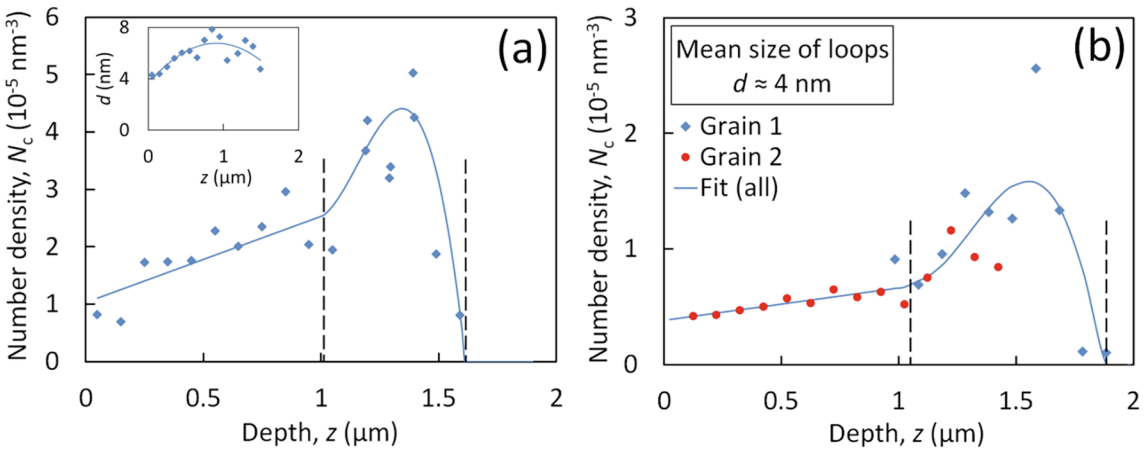

Fig. 5. Depth profile of the number density N_c of counted irradiation-induced dislocation loops. (a) Fe-9Cr, (b) ODS FeCr. The inset in (a) shows the mean size of loops as function of z.

the larger-z flank of the peak.

3.3. Nanoindentation

The measured indentation hardness is plotted in Fig. 8 as a function of contact depth [52]. The errors were derived from standard deviations of force and displacement. The curves for the unirradiated condition were fitted by proper empirical functions, see solid lines in the plots, in order to interpolate and calculate the irradiation-induced hardness increase.

3.4. Modelling of irradiation hardening

Conceptually, starting point is the yield stress $\sigma_{y,u}$ of the unirradiated material, which, in the present context, can be expressed as [39,49]:

$$\sigma_{y,u} = \sigma_{gb} + \sqrt{\sigma_f^2 + \sigma_p^2} \quad (2)$$

σ_{gb}, σ_f, and σ_p are contributions arising from grain boundaries, forest dislocations, and precipitates or oxide nanoparticles, respectively. It is important to note that Eq. (2), including its parameterization, was empirically confirmed in [49] for a number of ODS and non-ODS Fe-Cr-based alloys with the two materials of the present study included.

A spatially uniform irradiation field gives rise to the formation of dislocation loops and solute clusters or precipitates, which in turn "add" contributions σ_l and σ_c, respectively, to the yield stress $\sigma_{y,i}$ of the irradiated material. Plastic deformation of either the unirradiated or the irradiated material gives rise to the formation of geometrically necessary dislocations (GNDs) and statistically stored dislocations (SSDs). These dislocations, once formed, also "add" contributions σ_g and σ_s, respectively. While it is reasonable to sum up all contributions arising from dislocations (forest, GNDs, SSDs) in terms of the linear sum of the respective dislocation densities ρ_x (x = f, g or s), the type of superposition for irradiation-induced barriers were reported to depend on the ratio of barrier strengths and the ratio of number densities [38,41–43]. This is why we cover the two extreme cases, namely linear sum and square root of sum of squares, in the analysis.

The situation is significantly complicated for the case of ion irradiation and nanoindentation due to the introduction of steep damage gradients, strain gradients, related size effects, and possibly synergistic effects. In order to calculate the ion-irradiation-induced hardness increase from observations of the microstructure, we have applied combinations of the half-sphere model of the indentation plastic zone [24,25,29,30,32] and the DBH model [37,47] as approximations. The geometrical situation of the indentation test is schematically introduced in Fig. 9. The contact depth is denoted by h in both the scheme and the following equations. The radius of the plastic zone denoted by R is assumed to be proportional to h with c denoting the factor of proportionality. As an additional approximation, the same factor c is used for indentations in the irradiated and unirradiated material. We will come back to the justification of this approximation in Section 4.2.

According to the DBH model, the hardness contribution H arising from a single type of barrier of mean size d and number density N is

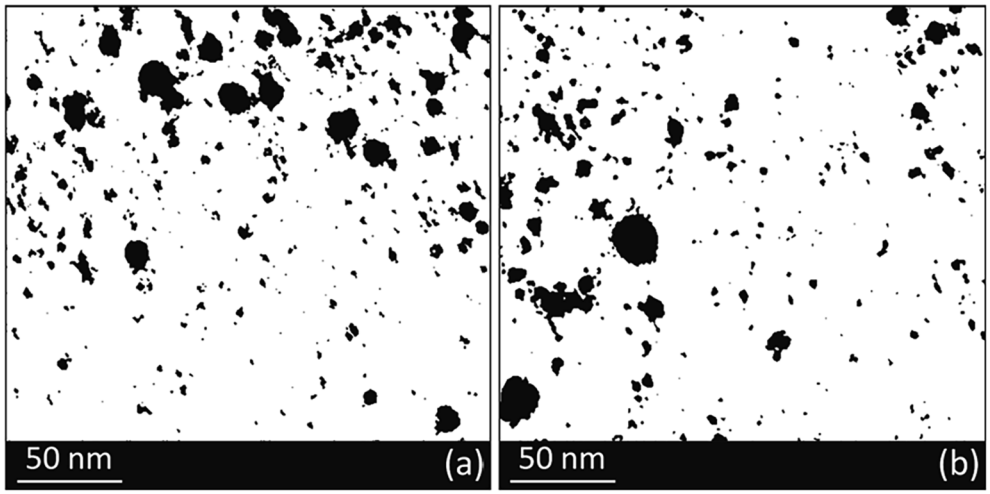

Fig. 6. Particle analysis based on TEM micrographs of ODS FeCr with loop contrast suppressed (see Fig. 3d) in order to highlight oxide nanoparticles, (a) unirradiated condition, lower dashed-line square in Fig. 3a, (b) ion irradiated condition, upper dashed-line square in Fig. 3a. The same image processing parameters including contrast enhancement and detection threshold were applied to (a) and (b).

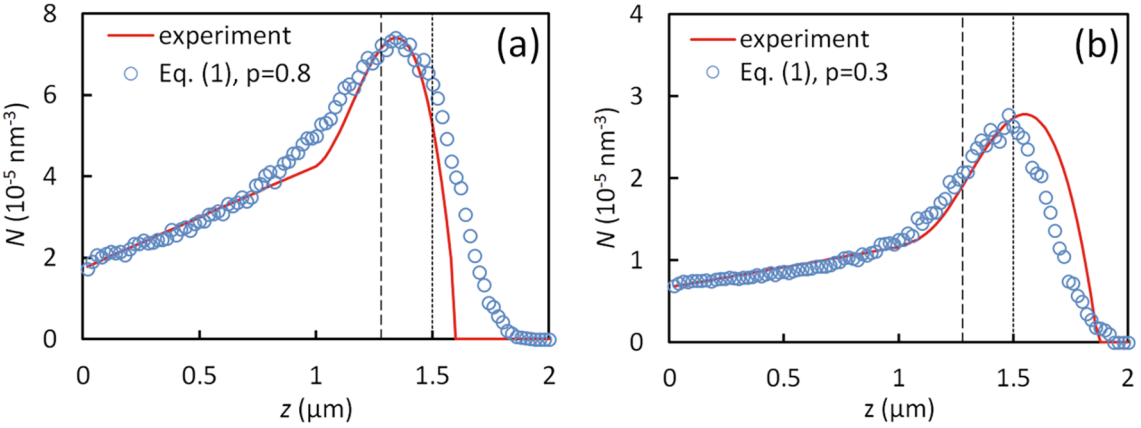

Fig. 7. Best fit according to Eq. (1) (symbols) to the measured number density of loops according to Fig. 5 (solid lines). (a) Fe-9Cr, (b) ODS FeCr. Dashed and dotted lines represent the depth at peak damage and maximum injected interstitials, respectively.

Table 4
Best values of the parameters of Eq. (1) derived by the heuristic approach.

Material	a_1	p	a_2
Fe-9Cr	1.38	0.8	940
ODS FeCr	0.54	0.3	570

given by Eq. (3).

$$H = \alpha\beta MGb\sqrt{Nd} \tag{3}$$

α, β, M, G and b are dimensionless obstacle strength, conversion factor from yield stress to bulk-equivalent indentation hardness, Taylor factor, shear modulus and Burgers vector, respectively.

In the case study below, we distinguish two possible rules of superposition of hardening contributions arising from pre-existing and irradiation-induced obstacles: linear sum (indicator "lin") and square root of sum of squares (indicator "srss"). For each of these rules, we further distinguish averaging of contributions arising from different volume elements of the plastic zone in terms of either hardness itself (indicator "h") or dislocation line length (indicator "d"), the latter being equivalent with averaging of the square of hardness. These distinctions result in the following four cases:

Case 1 (lin-h): For linear superposition of hardening contributions arising from pre-existing and irradiation-induced barriers (here loops), the pre-existing barriers drop out in the irradiation-induced change of hardness. The same is true for the GNDs introduced by indentations of equal depth, that means the indentation size effect. Averaging over different volume elements of the plastic zone is performed in terms of hardness ($\sqrt{\rho}$ or $\sqrt{\mathrm{Nd}}$).

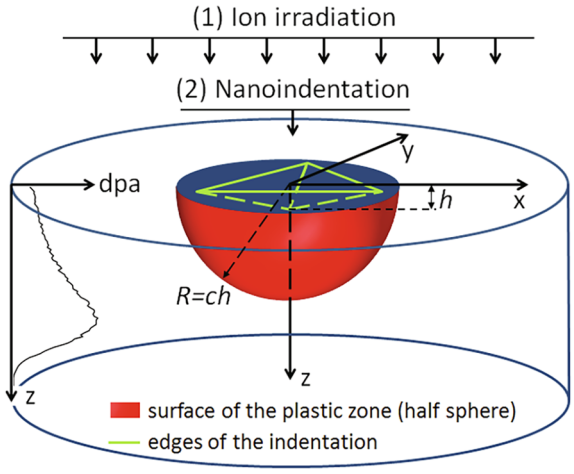

Fig. 9. Scheme representing the indentation into a sample with graded damage profile and the introduction of the coordinate system.

$$\Delta H(h) = \frac{\alpha_l \beta MGb}{V_{PZ}(h)} \int_{PZ(h)} \sqrt{N_l(z) d_l(z)}\, dV \tag{4a}$$

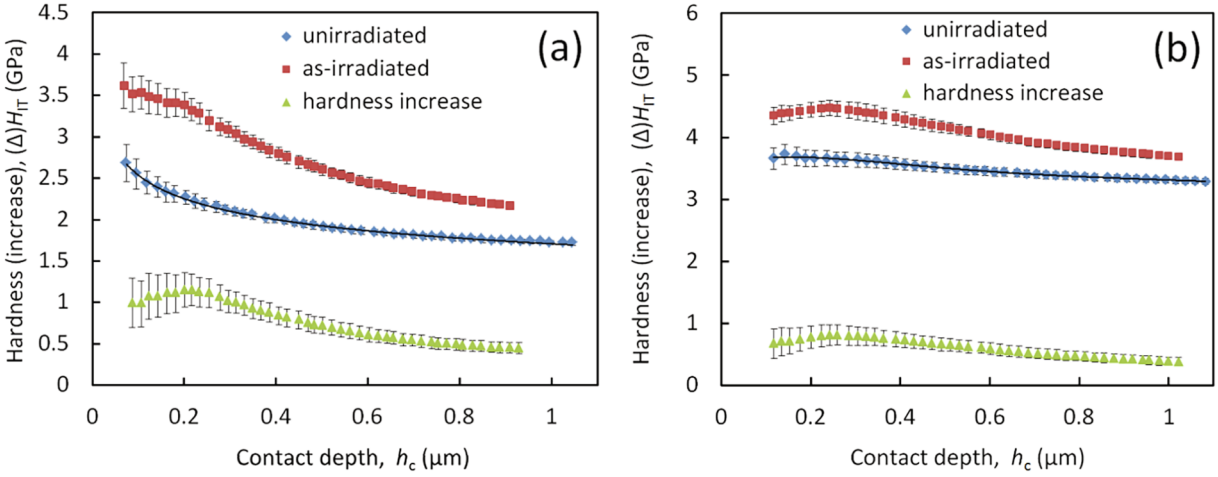

Fig. 8. Measured indentation hardness for the unirradiated and as-irradiated conditions and the difference of both. (a) Fe-9Cr, (b) ODS FeCr.

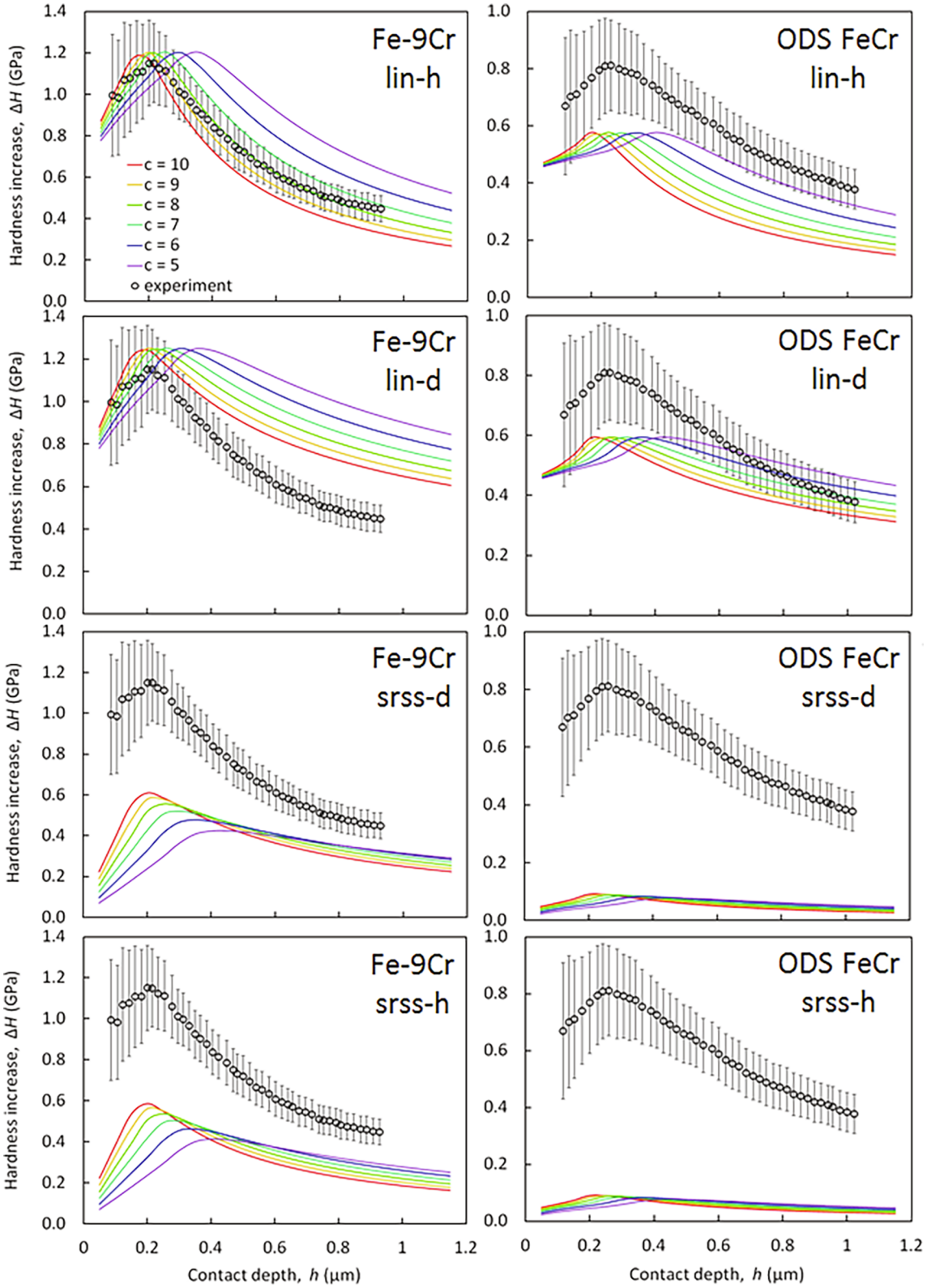

Fig. 10. Irradiation-induced hardness increase derived from NI tests (symbols) and calculated according to Cases 1 – 4 of the microstructure-informed model (coloured lines): Cases 1 to 4 from top to bottom. Numbers in the upper left plot indicate the value of c (see main text).

V is the volume and PZ indicates the indentation plastic zone. Execution of the integrations over x and y yields, assuming $h \ll R$, the following equation for the irradiation-induced hardness increase according to Case 1:

$$\Delta H(h) = \frac{3\alpha_1 \beta M G b}{2ch} \int_0^{ch} \left[1 - \frac{z^2}{(ch)^2}\right] \sqrt{N_1(z) d_1(z)}\, dz \tag{4b}$$

The parameterizations obtained for the experimentally observed number densities and mean sizes as functions of depth z (see solid lines

in Fig. 5) allow the integration according to Eq. (4b) to be executed for both materials. The following values of the model parameters were chosen: $\alpha_l = 0.33$ (for loops, e.g. [27,41]), $\beta = 4$ (estimated from the yield stress in Table 2 and the bulk-equivalent indentation hardness [21] of the unirradiated materials), $M = 3.06$, $G = 84.4$GPa [49,56], and $b = 0.248$nm. The effect of variations of these factors will be considered in the discussion. The factor of proportionality c between contact depth and radius of the half-sphere plastic zone was varied between 5 and 10 in steps of 1. The results are plotted in the first row of Fig. 10 along with the measured increase of the indentation hardness [52]. The values of c are indicated in the plots. It is important to note that the procedure is free of fitting. It is found that a substantial part of the measured hardening can be explained in terms of loops and that a value of $c = 8$ reproduces the depth position of the measured maximum hardening best.

In what follows, corresponding results are briefly summarized for the other three cases.

Case 2 (lin-d): At difference from Case 1, averaging over different volume elements of the plastic zone is performed in terms of dislocation line length (ρ or Nd, which correspond to the square of hardness), Eq. (5). The results are plotted in the second row of Fig. 10.

$$\Delta H(h) = \frac{\sqrt{3}\alpha_l \beta M G b}{\sqrt{2ch}} \sqrt{\int_0^{ch} \left[1 - \frac{z^2}{(ch)^2}\right] N_l(z) d_l(z) dz} \tag{5}$$

Case 3 (srss-d): At difference from Case 2, the irradiated hardness is assumed to be the square root of sum of squares of the unirradiated hardness and the irradiation-induced hardness contribution, Eqs. (6) and (7). Contrary to the case of linear superposition, the pre-existing obstacles (forest dislocations of density ρ_f, particles of number density N_p and mean diameter d_p) do not drop out in the irradiation-induced change of hardness. This is also valid for the GNDs of density ρ_g and SSDs of density ρ_s. The density of GNDs ρ_g was calculated according to Nix and Gao [29] assuming that GNDs are uniformly distributed over the plastic zone of radius R = ch. Note that, contrary to [29], we did neither introduce the characteristic length h* nor separate the ISE term. Instead, the indentation size effect is equivalently included in the term $\Omega(h)$.

$$\Delta H(h) = \alpha\beta M G b \left[\sqrt{\Omega + \frac{3}{2ch} \int_0^{ch} \left[1 - \frac{z^2}{(ch)^2}\right] N_l(z) d_l(z) dz} - \sqrt{\Omega} \right] \tag{6}$$

$$\Omega(h) = \rho_f + N_p d_p + \rho_s + \rho_g \text{ with } \rho_g = \frac{3}{2bhc^3 \tan\theta} \tag{7}$$

The expression for ρ_g was obtained as in [29], but taking into account a variable value of c, see Fig. 9, instead of $c = 2.79$ (plastic zone and indent coincide at the surface) assumed in [29]. This corresponds to the procedure suggested in [26]. For Eqs. (6) and (7), it is important to note that the average density of SSDs ρ_s does not depend on h [34]. ρ_s was assumed to be equal for the unirradiated and irradiated material in Eq. (6). Moreover, it was set to zero for the reported calculations. Introduction of SSDs of non-zero density would be equivalent to increasing ρ_f in the present framework. The same value of the obstacle strength, $\alpha = 0.33$, was used for dislocations [49,57] of any origin, oxide nanoparticles [49] and irradiation-induced dislocation loops (see above) as an approximation. The density of pre-existing dislocations and both number density and mean diameter of pre-existing particles were taken from Table 2. The results are shown in the third row of Fig. 10.

Case 4 (srss-h): At difference from Case 3 and in agreement with Case 1, averaging over different volume elements of the plastic zone is performed in terms of hardness, Eq. (8) with Eq. (7). The results are shown in the lowest row of Fig. 10.

$$\Delta H(h) = \frac{3\alpha\beta M G b}{2ch} \int_0^{ch} \left[1 - \frac{z^2}{(ch)^2}\right] \left(\sqrt{\Omega + N_l(z) d_l(z)} - \sqrt{\Omega}\right) dz \tag{8}$$

4. Discussion

In this section, the link between primary radiation damage and the irradiation-induced dislocation loops is considered first. The link between microstructure, in terms of irradiation-induced dislocation loops, and hardening established by the application of the microstructure-informed hardening model will be addressed in Section 4.2. Both the microstructure-informed "prediction" of hardening and the measured NI response exhibit maxima as functions of the indentation contact depth. In order to verify certain model assumptions, predictions and measurements will be compared with respect to the depth position of the maximum and to the slope of the curves towards larger contact depths (i.e. the substrate effect). It is important to note that deviations between prediction and measurement will not be interpreted, except for extreme deviations, with respect to the height of the maximum because of uncertainties of the model, in particular the omission of possible TEM-invisible hardening features. Because of uncertainties of the measurements at the lowest indentation depths, predictions and measurements will not be compared with respect to the slope towards smaller contact depths either. In Section 4.3, the predicted hardening will be decomposed into a component related to the loop fraction arising solely from the displacement damage and a component related to the loop fraction arising solely from the injected interstitials. The latter is irrelevant for the case of neutron irradiations and can be considered as an artefact [58]. Finally, the possible presence or absence of additional irradiation-induced hardening features will be addressed in Section 4.4.

4.1. Link between primary radiation damage and microstructure

The number density of irradiation-induced loops was successfully decomposed into fractions arising from the displacement damage and the injected interstitials according to Eq. (1). The first fraction can be approximately expressed as a power-law function of the displacement damage using the parameters listed in Table 4. Ignoring the minor effect of loop size, this is consistent with previous studies reporting applicability of a power-law dependence of the irradiation-induced increase of hardness (or yield stress) on displacement damage [24,25,45,46] with an exponent $q = p/2$, with p from Eq. (1). For Fe-9Cr, $q = 0.4$ is close to the frequently observed exponent of 0.5 at lower values of displacement damage [45]. The exponent $q = 0.15$ for ODS FeCr, which is significantly smaller than 0.5, indicates an advanced tendency towards saturation. This is also consistent with observations for an ODS 9%Cr steel as compared to its non-ODS counterpart [59]. These findings indicate that it is impossible to use a fixed universal value of p as occasionally done in the literature. Indeed, p depends on both the material and the considered domain of displacement damage.

The coefficients $a_2 = 940$ for Fe-9Cr and $a_2 = 570$ for ODS FeCr according to Eq. (1), see Table 4, can be converted into fractions of the total number of injected interstitials that contribute to the observed loops. Calculating the number of interstitials that constitute a loop of diameter d [60] and taking into account the observed mean diameters of loops, these fractions were found to be approximately 7% and 2% for Fe-9Cr and ODS FeCr, respectively. The lower fraction found for ODS FeCr correctly reflects the higher sink strength for point defect sinks [38] caused by the oxide nanoparticles in combination with the smaller grain size (see Table 2) as reported in [61]. The above estimation is based on the interpretation of the detected loops as interstitial-type loops. Very recently the loops detected under similar conditions were found to be vacancy-type [62]. This point deserves further attention.

It is important to note that there is a finite range of depths, where

the concentration of injected interstitials is negligibly small and the displacement damage is different from zero, see Fig. 2. As the injected interstitials pose a transferability issue to the case of neutron irradiation, it was suggested, on the one hand, to use sufficiently high ion energies, identify artefact-free or "safe" zones by way of microstructure studies, and restrict transfer of conclusions to these safe zones [4,58]. On the other hand, NI (as well as other methods such as depth-resolved positron annihilation spectroscopy [63]) integrates over a depth range from the irradiated surface up to a finite depth (for NI, the depth of the plastic zone), that means, over a range that can hardly be fully covered in practice by a safe zone. It is therefore a reasonable option from the viewpoint of NI to explicitly introduce the effects of injected interstitials into hardness modelling and analysis.

4.2. Link between irradiated microstructure and hardening

We have found that the measured irradiation-induced hardness change assumes maxima for certain values of the contact depth h, see Fig. 10. It is important to note that the error bars shown in Fig. 10 do not question the existence of such maxima. While these errors are representative for comparing, for example, different materials, the scatter of the individual data points with respect to an average ΔH-h curve is much smaller. The existence of a maximum of hardening as function of contact depth is expected as a consequence of the irradiation-induced microstructure. Indeed, each version of the microstructure-informed hardening model predicts a maximum, see Fig. 10. The interpolated positions of the measured maxima, h_{max}, are given in Table 5 for both materials. The model calculations indicate that the position of the maximum is shifted towards smaller indentation depths for increasing values of c, i.e. the size factor of the plastic zone. Agreement between the measured and predicted positions of the maxima, as determined by way of interpolation using the model Case 1 (lin-h), is reached for size factors, c_1, also provided in Table 5. These results do not differ significantly for Cases 1 to 4 of the model and are in general agreement with reported values or ranges of c (5 – 10 [20] and references therein, 8 [22], 7.5 [24], 5 – 8 [25]).

An approximation of the size factor can be obtained by applying the expanding cavity model [30] to the indentation plastic zone. The expression reported in [30] with the yield stresses from Table 2 (along with a Young's modulus of 210 GPa and a Poisson ratio of 0.28) yields the values of c_{ec} given in Table 5. The experimentally obtained size factors c_1 are found to be slightly overestimated by the expanding cavity model, for Fe-9Cr more than for ODS FeCr. This may be a consequence of the strain-hardening capacity of the studied materials indicated in Table 5 in terms of reported values of the uniform elongation, the fractional value of which corresponds to the strain hardening exponent. Because of strain hardening, which is not taken into account in the expanding cavity model, the materials appear harder, the more so for Fe-9Cr, than what is indicated by the yield stress, tentatively explaining the observed overestimation. Further work is necessary to refine the model in this respect.

It is important for the applied microstructure-informed model to note that the dependence of the size factor c_1 on the yield stress is weak, in any case weaker than predicted by the expanding cavity model. Indeed, the yield stress of ODS FeCr (720 MPa) is 2.5 times as large as the yield stress of Fe-9Cr (289 MPa), whereas the corresponding factor for the plastic zone size was found to be approximately 7.5/8.5 = 0.88. This result has two consequences: (i) The shape of the plastic zone of the irradiated materials may deviate from a half sphere because of the depth-dependent irradiation hardening. However, this deviation is small, in any case smaller than predicted by the expanding cavity model. (ii) The plastic zone size of the irradiated material may deviate from the plastic zone size of the unirradiated reference. However, this deviation is also small, in any case smaller than predicted by the expanding cavity model. These findings justify the approximations of both the half-sphere shape of the plastic zone and the equality of the sizes for the irradiated and unirradiated materials introduced in Section 3.4.

Table 5
Experimentally determined depth position of maximum hardness increase, size factor c_1 that fits the position of the maximum predicted within Case 1 (lin-h) to the experiment, size factor c_{ec} according to [30] and reported uniform elongation A_g.

Material	h_{max} (μm)	c_1 (–)	c_{ec} (–)	A_g (%)
Fe-9Cr	0.21 ± 0.02	8.5 ± 0.5	11.0	15 [48]
ODS FeCr	0.26 ± 0.02	7.5 ± 0.5	8.1	10 [49]

The individual results obtained for the considered model versions, see Fig. 10, are discussed below case by case:

Case 1 (lin-h): There is agreement within the range of experimental error between measurement and microstructure-informed prediction for Fe-9Cr using c = 8 throughout the entire range of contact depths. In particular, the slope of the ΔH-h_c curve towards larger h_c, that means, the substrate effect, is well reproduced by the prediction. However, the agreement between measured and predicted values of ΔH has to be assessed as being coincidental. Expected deviations resulting from measurement errors, possible additional hardening contributions, model assumptions, and model parameterization (see Section 4.4) seem to cancel out.

For ODS FeCr, the measured hardening is well reproduced by the model with respect to the existence and, for a size factor between 7 and 8, the depth position of the maximum as well as the substrate effect. The measured hardening is underestimated by approximately 30%, which is more than the error of the measured hardening, see Section 4.4.

Case 2 (lin-d): The microstructure-informed model predicts positions of the maxima similar to those observed for Case 1 for both Fe-9Cr and ODS FeCr. However, the predicted slope towards larger values of the contact depth is significantly smaller than the measured slope for both materials, that means, the substrate effect is not well reproduced. We conclude that averaging dislocation line length (or Nd) instead of hardness (or square root of Nd) over the plastic zone is not consistent with the present observations and model assumptions of Case 2. Presumably, the assumptions of linear superposition and averaging dislocation line length are incompatible. A prediction equivalent to Case 2 was also considered in [23,26] as a reference case (denoted Model I there). These authors found by way of fitting that the substrate effect cannot be reproduced well, in agreement with the present finding for both materials. Interestingly, averaging the dislocation line length according to Case 2 was successfully applied in [9] for ion-irradiated austenitic stainless steels. However, these authors only reported hardening for a single indentation depth. The depth dependence of the measured hardening was not available for verifying their assumptions. Given the approximations included in [9], comparison of measurement and prediction for just a single value of indentation depth is insufficient for a sound assessment of the validity of the assumptions.

Case 3 (srss-d): For Fe-9Cr, the measured hardening is well reproduced by the model with respect to the existence and, for a size factor between 8 and 9, the depth position of the maximum as well as the substrate effect. The measured hardening is underestimated by approximately 50%, see Section 4.4. The underestimation observed in the framework of Case 3 for ODS FeCr is more drastic than for Fe-9Cr and amounts to a factor of approximately 10. It is interesting to compare our findings for Case 3 with reported results [23,26] based on both the same type of superposition of the hardening contributions and the same type of averaging the hardening contributions arising from different volume elements (see [23,26] and Model II in [26]). In [23,26] as well as in our work, the treatments of the indentation size effect are equivalent and the plastic zone is assumed to be a half-sphere of equal size for the unirradiated and irradiated condition with a size factor of 7.5 used in [23,26]. However, the latter studies did not build on own

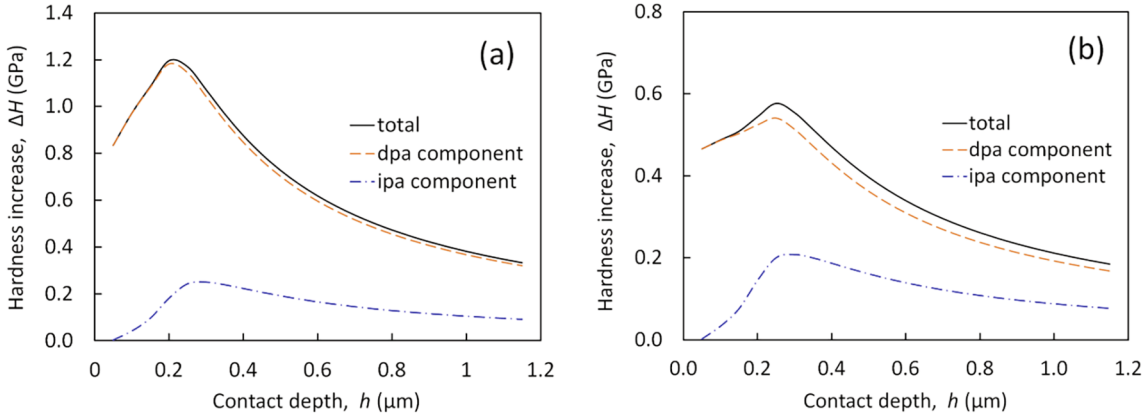

Fig. 11. Decomposition of the predicted hardening (Case 1: lin-h) into contributions arising solely from displacement damage and solely from injected interstitials according to Eqs. (1) and (4b) for (a) Fe-9Cr, (b) ODS FeCr. Parameters according to Table 4, $c = 8$.

microstructural evidence representative of the samples exposed to NI. Instead, these authors assumed a power-law dependence of the number density of defects on depth with exponents and cut-off depths used to fit the measured hardness. Given the multitude of simplifying assumptions, just successful fitting is insufficient, in our opinion, as a means to validate the model.

Case 4 (srss-h): The prediction based on Case 4 is almost indistinguishable from the prediction based on Case 3 except for small differences at the largest contact depths for Fe-9Cr. Hence, for srss-type superposition, the question of averaging the dislocation line length or the hardness over the plastic zone cannot be decided within the present framework.

4.3. Link between primary radiation damage and hardening

With the results of Sections 3.2 and 3.4 at hand, it is possible to decompose the predicted hardening into contributions arising from the loops formed due to either displacement damage or clustering of injected self-interstitial atoms considered as independent processes. This decomposition was conducted for Case 1 (lin-h) using Eqs. (1) and (4b) along with the parameters given in Table 4 and assuming a plastic zone size factor of 8 for both materials. The results are shown in Fig. 11. The total number density of loops was supposed, according to Eq. (1), to be the linear sum of both contributions, meaning that the total predicted hardness is the square root of sum of squares of the individual contributions in terms of hardness (dpa and ipa in Fig. 11). This should not be confused with the linear superposition of the unirradiated hardness and the irradiation hardening.

It is well known that there are several transferability issues with respect to the application of ion irradiations in order to emulate effects of neutron irradiation [64]. One of these issues consists in the effect of injected interstitials, which are not introduced in the case of neutron irradiation. Therefore, it is the dpa component in Fig. 11 that matters from the viewpoint of reactor applications, while the ipa component can be considered as artefact. The results suggest that, although the effect of the injected interstitials is significant, the dpa component of hardening is close to the total hardening because of the srss-type of superposition of both components. Conversely, close agreement between the dpa component and the total hardening must not be misinterpreted as an implication that injected interstitials did not contribute to hardening. Moreover, injected interstitials may play a more important role for other irradiation conditions, e.g. lower ion energy or other kinds of ions. Ongoing research is focused on the effect of the ion energy.

4.4. Other potential hardening features

The TEM analyses performed within the present study did not reveal any other kinds of irradiation-induced features than loops. However, this observation does not exclude their possible presence. As already pointed out, the present study was not aimed at providing a complete quantitative prediction of the measured NI response. In fact, a complete microstructure-informed model would require a complete description of all irradiation-induced nanostructural changes including the depth dependence of their characteristics. Theoretically, candidates for such changes under the present conditions are the formation of solute atom clusters, Cr-rich α'-phase particles, nanovoids or sub-nm vacancy clusters, and changes of the size distribution of oxide nanoparticles. Loops of size below the detectability limit of TEM (between 1 and 2 nm) also have to be mentioned here.

The present TEM investigation was well suited to exclude changes of the size and number density of oxide nanoparticles in excess of the observed spatial variations, see Fig. 6 and the related discussion. Noticeable effects on the irradiation-induced hardness change of ODS FeCr can therefore be excluded. A noticeable contribution of α'-phase particles can be excluded for both materials based on the combination of the following three arguments: (a) Supersaturation at 300 °C is small for the studied materials [65]. (b) The injected interstitials were reported to suppress α′ formation when compared to the case of neutron irradiation [12]. (c) The barrier strength α according to Eq. (3) was reported to be as small as 0.015 [56]. So even if a small number density of α′-phase particles were formed, the contribution to hardening can also be neglected. While precipitates (e.g. Si-Ni-Mn-rich G-phase particles [66,67]) and nanovoids of size in excess of a few nm can also be excluded on the basis of the presented TEM evidence, nm-sized solute atom clusters (e.g. highly diluted Ni-Si-P-Cr-rich clusters [13]) and sub-nm vacancy clusters [68] cannot. In fact, depth-resolved versions of other methods such as atom probe tomography (APT) [12] and positron annihilation spectroscopy (PAS) [63] are needed to identify missing defects or to convincingly exclude their presence. At least for neutron-irradiated Fe-9Cr, even the formation of sub-nm vacancy clusters was found by means of PAS to be completely suppressed due to the presence of Cr [68]. In summary, nm-sized solute atom clusters are the only reasonable candidates for possible contributions to the observed irradiation-induced hardness increase. However, their depth distribution, which is governed by the depth-dependent displacement damage [13], is expected to result in an approximately proportional elevation of the respective ΔH-h curve (green dashed lines in Fig. 11) without noticeable change of the shape including the position of the maximum.

4.5. Superposition rules

Even being aware of the missing pieces of information as outlined above, it is surprising that the microstructure-informed model with srss-type superposition, which, according to [26], is more promising than linear superposition, gives rise to an underestimation of the NI response for ODS FeCr by an order of magnitude. This can hardly be explained by possibly missing TEM-invisible hardening features. It cannot be explained by the approximations due to the model parameterization either. Tentatively, we have to conclude that linear superposition is more appropriate for ODS FeCr contrary to the reported opinion, e.g. [26]. This is at difference from the situation for Fe-9Cr, for which, taking into account possibly missing hardening features, neither linear nor srss-type superposition (nor anything in between) is in conflict with the measured NI response. Indeed, mixed linear/srss-type superposition [42] and superposition rules with fractional exponent between 1 (linear) and 2 (srss) [36] were suggested in the literature.

The difference between the superposition rules found to be appropriate for the two materials is presumably due to the ratio of irradiation hardening and initial hardness. This ratio is approximately 1/2 and 1/5 for Fe-9Cr and ODS FeCr, respectively, see Fig. 8. In terms of microstructure, the most prominent difference is the presence of oxide nanoparticles in ODS FeCr, which alone make up more than 50% of the initial hardness.

5. Conclusions

The depth-dependent distribution of dislocation loops and the nanohardness as a function of contact depth were measured for Fe-9Cr and ODS FeCr irradiated with 5 MeV Fe ions. Empirical models were applied to link primary radiation damage with the irradiated microstructure and the microstructure with irradiation hardening.

TEM revealed visible bands of increased number density of loops in the depth range around maximum dpa and maximum injected interstitials. The experimentally determined depth-dependent number density of dislocation loops was decomposed into fractions arising from displacement damage and injected interstitials. The latter fraction corresponds to 7% and 2% of the total injected interstitials for Fe-9Cr and ODS FeCr, respectively. The lower fraction for ODS FeCr is consistent with the operation of oxide nanoparticles as point-defect sinks.

For both materials, a maximum of the irradiation-induced hardness increase as a function of contact depth was found. This observation is rationalized by a combination of the dispersed barrier hardening model and the half-sphere approximation of the plastic zone. The predicted and observed positions of the maximum were found to agree for size factors of the plastic zone of 8.5 and 7.5 for Fe-9Cr and ODS FeCr, respectively. The size factors calculated according to the expanding cavity model [30] overestimate our values, but follow the same ranking. The overestimation can be explained by strain hardening not considered in the expanding cavity model.

The amount of predicted irradiation hardening depends on the selected superposition rule of contributions arising from pre-existing and irradiation-induced barriers. For linear superposition, the substrate effect is correctly reproduced by averaging the hardness over the plastic zone, but not by averaging the square of hardness (i.e. the dislocation density). No such discrimination was found for srss-type superposition. Tentatively, the appropriate superposition rule is found to be between linear and srss for Fe-9Cr and close to linear for ODS FeCr. This difference is presumably due to different ratios of irradiation hardening and initial hardness. The inappropriateness of srss-type superposition for ODS FeCr is surprising and requires further attention.

The presented framework is useful for the separation of the pure effect of displacement damage from the total ion-irradiation effect on hardening as a step towards improved transferability to the case of neutron irradiation hardening. It is important to note that this is only one out of several transferability issues also including effects of steep damage gradients, pulsed versus continuous irradiation and irradiation flux.

Important subjects of ongoing and future work are a more complete characterization of the irradiated microstructure, including atom probe tomography, of the investigated alloys as well as the consideration of model alloys that exhibit only one type of irradiation-induced nano-features. Such studies will allow microstructure-informed predictions and the measured NI response to be compared with respect to the absolute value of hardening. Ongoing work is also dedicated to the effect of the ion energy on irradiated microstructures and hardening.

CRediT authorship contribution statement

K. Vogel: Conceptualization, Methodology, Formal analysis, Investigation, Visualization, Writing - review & editing. **C. Heintze:** Conceptualization, Methodology, Formal analysis, Investigation, Visualization, Writing - review & editing, Supervision, Funding acquisition. **P. Chekhonin:** Methodology, Software, Validation, Writing - review & editing. **S. Akhmadaliev:** Formal analysis, Investigation, Resources, Writing - review & editing. **E. Altstadt:** Formal analysis, Writing - review & editing, Project administration, Funding acquisition. **F. Bergner:** Conceptualization, Methodology, Formal analysis, Writing - original draft, Writing - review & editing, Visualization, Supervision, Funding acquisition.

Declaration of Competing Interest

The authors declare that they have no known competing financial interests or personal relationships that could have appeared to influence the work reported in this paper.

Acknowledgements

This work received partial funding by the European Commission within the projects MATISSE (Grant Agreement No. 604862) and M4F (Grant Agreement No. 755039). The transmission electron microscope Talos was funded by the German Federal Ministry of Education and Research (BMBF) (Grant No. 03SF0451) in the framework of the Helmholtz Energy Materials Characterization Platform (HEMCP). The ion irradiations were carried out at the Ion Beam Center at Helmholtz-Zentrum Dresden-Rossendorf. The work contributes to the Joint Programme on Nuclear Materials (JPNM) within the European Energy Research Alliance (EERA). The authors wish to thank M. Hernández Mayoral and M. Gonzales Castaño for helpful comments and the preparation of the plan-view sample. Surface preparation by M. Roßner and FIB sample preparation by A. Kunz are also gratefully acknowledged.

Data availability

The raw/processed data required to reproduce these findings are included in the dataset [52]. The access to the dataset is restricted, access right will be provided on request.

References

[1] J.F. Ziegler, M.D. Ziegler, J.P. Biersack, SRIM – The stopping and range of ions in matter (2010), Nucl. Instrum. Methods Phys. Res. Sect. B Beam Interact. Mater. At. 268 (2010) 1818–1823. DOI:10.1016/j.nimb.2010.02.091.

[2] R.E. Stoller, M.B. Toloczko, G.S. Was, A.G. Certain, S. Dwaraknath, F.A. Garner, On the use of SRIM for computing radiation damage exposure, Nucl. Instrum. Methods Phys. Res. Sect. B Beam Interact. Mater. At. 310 (2013) 75–80, https://doi.org/10.1016/j.nimb.2013.05.008.

[3] K. Nordlund, S.J. Zinkle, A.E. Sand, F. Granberg, R.S. Averback, R.E. Stoller, T. Suzudo, L. Malerba, F. Banhart, W.J. Weber, F. Willaime, S.L. Dudarev, D. Simeone, Primary radiation damage: a review of current understanding and models, J. Nucl. Mater. 512 (2018) 450–479, https://doi.org/10.1016/j.jnucmat.2018.10.027.

[4] P.J. Doyle, K.M. Benensky, S.J. Zinkle, Modeling the impact of radiation-enhanced diffusion on implanted ion profiles, J. Nucl. Mater. 509 (2018) 168–180, https://doi.org/10.1016/j.jnucmat.2018.06.042.

[5] L.L. Horton, J. Bentley, W.A. Jesser, The microstructure of “triple-beam” ion irradiated Fe and Fe-Cr alloys, J. Nucl. Mater. 104 (1981) 1085–1089, https://doi.org/10.1016/0022-3115(82)90745-0.

[6] J. Gao, K. Yabuuchi, A. Kimura, Characterization of ordered dislocation loop raft in Fe3+ irradiated pure iron at 300 °C, J. Nucl. Mater. 511 (2018) 304–311, https://doi.org/10.1016/j.jnucmat.2018.09.020.

[7] C. Shin, H. Jin, M.-W. Kim, Evaluation of the depth-dependent yield strength of a nanoindented ion-irradiated Fe–Cr model alloy by using a finite element modeling, J. Nucl. Mater. 392 (2009) 476–481, https://doi.org/10.1016/j.jnucmat.2009.04.011.

[8] K. Yutani, R. Kasada, H. Kishimoto, A. Kimura, R. Lott, S.W. Dean, Irradiation hardening and microstructure evolution of ion-irradiated ODS ferritic steels, J. ASTM Int. 4 (2007) 100701, , https://doi.org/10.1520/JAI100701.

[9] C. Liu, C. Yu, N. Hashimoto, S. Ohnuki, M. Ando, K. Shiba, S. Jitsukawa, Microstructure and micro-hardness of ODS steels after ion irradiation, J. Nucl. Mater. 417 (2011) 270–273, https://doi.org/10.1016/j.jnucmat.2011.01.067.

[10] D. Chen, K. Murakami, K. Dohi, K. Nishida, N. Soneda, Z. Li, L. Liu, N. Sekimura, Depth distribution of Frank loop defects formed in ion-irradiated stainless steel and its dependence on Si addition, Nucl. Instrum. Methods Phys. Res. Sect. B Beam Interact. Mater. At. 365 (2015) 503–508, https://doi.org/10.1016/j.nimb.2015.08.029.

[11] S.V. Rogozhkin, A.A. Nikitin, A.A. Khomich, A.A. Lukyanchuk, O.A. Raznitsyn, A.S. Shutov, P.A. Fedin, T.V. Kulevoy, A.L. Vasiliev, M.Yu. Presnyakov, A. Möslang, R. Lindau, P. Vladimirov, The influence of Fe-ion irradiation on the microstructure of reduced activation ferritic-martensitic steel Eurofer 97, Nucl. Fusion 59 (2019) 086018, , https://doi.org/10.1088/1741-4326/ab1e18.

[12] O. Tissot, C. Pareige, E. Meslin, B. Décamps, J. Henry, Influence of injected interstitials on α′ precipitation in Fe–Cr alloys under self-ion irradiation, Mater. Res. Lett. 5 (2017) 117–123, https://doi.org/10.1080/21663831.2016.1230896.

[13] C. Pareige, V. Kuksenko, P. Pareige, Behaviour of P, Si, Ni impurities and Cr in self ion irradiated Fe–Cr alloys – comparison to neutron irradiation, J. Nucl. Mater. 456 (2015) 471–476, https://doi.org/10.1016/j.jnucmat.2014.10.024.

[14] J.P. Wharry, M.J. Swenson, K.H. Yano, A review of the irradiation evolution of dispersed oxide nanoparticles in the b.c.c. Fe-Cr system: current understanding and future directions, J. Nucl. Mater. 486 (2017) 11–20, https://doi.org/10.1016/j.jnucmat.2017.01.009.

[15] P. Hosemann, D. Kiener, Y. Wang, S.A. Maloy, Issues to consider using nano indentation on shallow ion beam irradiated materials, J. Nucl. Mater. 425 (2012) 136–139, https://doi.org/10.1016/j.jnucmat.2011.11.070.

[16] C. Robertson, B.K. Panigrahi, S. Balaji, S. Kataria, Y. Serruys, M.-H. Mathon, C.S. Sundar, Particle stability in model ODS steel irradiated up to 100dpa at 600°C: TEM and nano-indentation investigation, J. Nucl. Mater. 426 (2012) 240–246, https://doi.org/10.1016/j.jnucmat.2012.04.001.

[17] C.D. Hardie, S.G. Roberts, Nanoindentation of model Fe–Cr alloys with self-ion irradiation, J. Nucl. Mater. 433 (2013) 174–179, https://doi.org/10.1016/j.jnucmat.2012.09.003.

[18] Y. Takayama, R. Kasada, Y. Sakamoto, K. Yabuuchi, A. Kimura, M. Ando, D. Hamaguchi, H. Tanigawa, Nanoindentation hardness and its extrapolation to bulk-equivalent hardness of F82H steels after single- and dual-ion beam irradiation, J. Nucl. Mater. 442 (2013) S23–S27, https://doi.org/10.1016/j.jnucmat.2012.12.033.

[19] R. Kasada, S. Konishi, K. Yabuuchi, S. Nogami, M. Ando, D. Hamaguchi, H. Tanigawa, Depth-dependent nanoindentation hardness of reduced-activation ferritic steels after MeV Fe-ion irradiation, Fusion Eng. Des. 89 (2014) 1637–1641, https://doi.org/10.1016/j.fusengdes.2014.03.068.

[20] C.K. Dolph, D.J. da Silva, M.J. Swenson, J.P. Wharry, Plastic zone size for nanoindentation of irradiated Fe–9%Cr ODS, J. Nucl. Mater. 481 (2016) 33–45, https://doi.org/10.1016/j.jnucmat.2016.08.033.

[21] C. Heintze, F. Bergner, S. Akhmadaliev, E. Altstadt, Ion irradiation combined with nanoindentation as a screening test procedure for irradiation hardening, J. Nucl. Mater. 472 (2016) 196–205, https://doi.org/10.1016/j.jnucmat.2015.07.023.

[22] M. Saleh, Z. Zaidi, M. Ionescu, C. Hurt, K. Short, J. Daniels, P. Munroe, L. Edwards, D. Bhattacharyya, Relationship between damage and hardness profiles in ion irradiated SS316 using nanoindentation – experiments and modelling, Int. J. Plast. 86 (2016) 151–169, https://doi.org/10.1016/j.ijplas.2016.08.006.

[23] X. Xiao, Q. Chen, H. Yang, H. Duan, J. Qu, A mechanistic model for depth-dependent hardness of ion irradiated metals, J. Nucl. Mater. 485 (2017) 80–89, https://doi.org/10.1016/j.jnucmat.2016.12.039.

[24] A. Kareer, A. Prasitthipayong, D. Krumwiede, D.M. Collins, P. Hosemann, S.G. Roberts, An analytical method to extract irradiation hardening from nanoindentation hardness-depth curves, J. Nucl. Mater. 498 (2018) 274–281, https://doi.org/10.1016/j.jnucmat.2017.10.049.

[25] F. Röder, C. Heintze, S. Pecko, S. Akhmadaliev, F. Bergner, A. Ulbricht, E. Altstadt, Nanoindentation of ion-irradiated reactor pressure vessel steels – model-based interpretation and comparison with neutron irradiation, Philos. Mag. 98 (2018) 911–933, https://doi.org/10.1080/14786435.2018.1425007.

[26] X. Xiao, L. Yu, Comparison of linear and square superposition hardening models for the surface nanoindentation of ion-irradiated materials, J. Nucl. Mater. 503 (2018) 110–115, https://doi.org/10.1016/j.jnucmat.2018.02.047.

[27] J. Gao, K. Yabuuchi, A. Kimura, Ion-irradiation hardening and microstructural evolution in F82H and ferritic alloys, J. Nucl. Mater. 515 (2019) 294–302, https://doi.org/10.1016/j.jnucmat.2018.12.047.

[28] X. Xiao, L. Yu, Nano-indentation of ion-irradiated nuclear structural materials: a review, Nucl. Mater. Energy 22 (2020) 100721, , https://doi.org/10.1016/j.nme.2019.100721.

[29] W.D. Nix, H. Gao, Indentation size effects in crystalline materials: a law for strain gradient plasticity, J. Mech. Phys. Solids 46 (1998) 411–425, https://doi.org/10.1016/S0022-5096(97)00086-0.

[30] K.L. Johnson, The correlation of indentation experiments, J. Mech. Phys. Solids 18 (1970) 115–126, https://doi.org/10.1016/0022-5096(70)90029-3.

[31] H.-S. Kim, D.-H. Lee, M.-Y. Seok, Y. Zhao, W.-J. Kim, D. Kwon, H.-H. Jin, J. Kwon, J. Jang, A novel way to estimate the nanoindentation hardness of only-irradiated layer and its application to ion irradiated Fe-12Cr alloy, J. Nucl. Mater. 487 (2017) 343–347, https://doi.org/10.1016/j.jnucmat.2017.02.028.

[32] D. Kiener, R. Pippan, C. Motz, H. Kreuzer, Microstructural evolution of the deformed volume beneath microindents in tungsten and copper, Acta Mater. 54 (2006) 2801–2811, https://doi.org/10.1016/j.actamat.2006.02.024.

[33] G. Voyiadjis, M. Yaghoobi, Review of nanoindentation size effect: experiments and atomistic simulation, Crystals 7 (2017) 321, https://doi.org/10.3390/cryst7100321.

[34] A. Ruiz-Moreno, P. Hähner, Indentation size effects of ferritic/martensitic steels: a comparative experimental and modelling study, Mater. Des. 145 (2018) 168–180, https://doi.org/10.1016/j.matdes.2018.02.064.

[35] A. Ruiz-Moreno, P. Hähner, L. Kurpaska, J. Jagielski, P. Spätig, M. Trebala, S.-P. Hannula, S. Merino, G. de Diego, H. Namburi, O. Libera, D. Terentyev, T. Khvan, C. Heintze, N. Jennett, Round robin into best practices for the determination of indentation size effects, Nanomaterials 10 (2020) 130, https://doi.org/10.3390/nano10010130.

[36] A.J. Ardell, Precipitation hardening, Metall. Trans. A 16 (1985) 2131–2165, https://doi.org/10.1007/BF02670416.

[37] S.J. Zinkle, Y. Matsukawa, Observation and analysis of defect cluster production and interactions with dislocations, J. Nucl. Mater. 329–333 (2004) 88–96, https://doi.org/10.1016/j.jnucmat.2004.04.298.

[38] G.S. Was, Fundamentals of Radiation Materials Science: Metals and Alloys, Springer, Berlin; New York, 2007.

[39] G. Monnet, Multiscale modeling of irradiation hardening: application to important nuclear materials, J. Nucl. Mater. 508 (2018) 609–627, https://doi.org/10.1016/j.jnucmat.2018.06.020.

[40] X. Xiao, Fundamental mechanisms for irradiation-hardening and embrittlement: a review, Metals 9 (2019) 1132, https://doi.org/10.3390/met9101132.

[41] A.J.E. Foreman, M.J. Makin, Dislocation movement through random arrays of obstacles, Can. J. Phys. 45 (1967) 511–517, https://doi.org/10.1139/p67-044.

[42] G.R. Odette, G.E. Lucas, Recent progress in understanding reactor pressure vessel steel embrittlement, Radiat. Eff. Defects Solids 144 (1998) 189–231, https://doi.org/10.1080/10420159808229676.

[43] M. Hiratani, V.V. Bulatov, Solid-solution hardening by point-like obstacles of different kinds, Philos. Mag. Lett. 84 (2004) 461–470, https://doi.org/10.1080/09500830410001726969.

[44] Y. Dong, T. Nogaret, W.A. Curtin, Scaling of dislocation strengthening by multiple obstacle types, Metall. Mater. Trans. A 41 (2010) 1954–1960, https://doi.org/10.1007/s11661-010-0229-z.

[45] K. Farrell, T.S. Byun, Tensile properties of ferritic/martensitic steels irradiated in HFIR, and comparison with spallation irradiation data, J. Nucl. Mater. 318 (2003) 274–282, https://doi.org/10.1016/S0022-3115(03)00102-8.

[46] T.S. Byun, K. Farrell, Irradiation hardening behavior of polycrystalline metals after low temperature irradiation, J. Nucl. Mater. 326 (2004) 86–96, https://doi.org/10.1016/j.jnucmat.2003.12.012.

[47] Seeger, Alfred, K., On the theory of radiation damage and radiation hardening, in: Second U. N. Int. Conf. Peac. Uses At. Energy, United Nations, New York, Geneva, Switzerland, 1958, pp. 250–273.

[48] M. Matijasevic, A. Almazouzi, Effect of Cr on the mechanical properties and microstructure of Fe–Cr model alloys after n-irradiation, J. Nucl. Mater. 377 (2008) 147–154, https://doi.org/10.1016/j.jnucmat.2008.02.061.

[49] A. Chauhan, F. Bergner, A. Etienne, J. Aktaa, Y. de Carlan, C. Heintze, D. Litvinov, M. Hernandez-Mayoral, E. Oñorbe, B. Radiguet, A. Ulbricht, Microstructure characterization and strengthening mechanisms of oxide dispersion strengthened (ODS) Fe-9%Cr and Fe-14%Cr extruded bars, J. Nucl. Mater. 495 (2017) 6–19, https://doi.org/10.1016/j.jnucmat.2017.07.060.

[50] M. Hernández-Mayoral, C. Heintze, E. Oñorbe, Transmission electron microscopy investigation of the microstructure of Fe–Cr alloys induced by neutron and ion irradiation at 300 °C, J. Nucl. Mater. 474 (2016) 88–98, https://doi.org/10.1016/j.jnucmat.2016.03.002.

[51] G. Brauer, W. Anwand, W. Skorupa, J. Kuriplach, O. Melikhova, C. Moisson, H. von Wenckstern, H. Schmidt, M. Lorenz, M. Grundmann, Defects in virgin and N + -implanted ZnO single crystals studied by positron annihilation, Hall effect, and deep-level transient spectroscopy, Phys. Rev. B 74 (2006), https://doi.org/10.1103/PhysRevB.74.045208.

[52] K. Vogel, C. Heintze, P. Chekhonin, S. Akhmadaliev, E. Altstadt, F. Bergner, Dataset on Relationships between primary radiation damage, irradiation-induced microstructure and hardening of ion-irradiated Fe-Cr and ODS Fe-Cr alloys, (2019). DOI:10.14278/rodare.184.

[53] A. Prokhodtseva, B. Décamps, A. Ramar, R. Schäublin, Impact of He and Cr on defect accumulation in ion-irradiated ultrahigh-purity Fe(Cr) alloys, Acta Mater. 61 (2013) 6958–6971, https://doi.org/10.1016/j.actamat.2013.08.007.

[54] W.C. Oliver, G.M. Pharr, An improved technique for determining hardness and elastic modulus using load and displacement sensing indentation experiments, J. Mater. Res. 7 (1992) 1564–1583, https://doi.org/10.1557/JMR.1992.1564.

[55] X. Li, B. Bhushan, A review of nanoindentation continuous stiffness measurement technique and its applications, Mater. Charact. 48 (2002) 11–36, https://doi.org/

10.1016/S1044-5803(02)00192-4.
[56] F. Bergner, C. Pareige, M. Hernandez-Mayoral, L. Malerba, C. Heintze, Application of a three-feature dispersed-barrier hardening model to neutron-irradiated Fe-Cr model alloys, J. Nucl. Mater. 448 (2014) 96–102, https://doi.org/10.1016/j.jnucmat.2014.01.024.
[57] M. Praud, F. Mompiou, J. Malaplate, D. Caillard, J. Garnier, A. Steckmeyer, B. Fournier, Study of the deformation mechanisms in a Fe–14% Cr ODS alloy, J. Nucl. Mater. 428 (2012) 90–97, https://doi.org/10.1016/j.jnucmat.2011.10.046.
[58] S.J. Zinkle, L.L. Snead, Opportunities and limitations for ion beams in radiation effects studies: bridging critical gaps between charged particle and neutron irradiations, Scr. Mater. 143 (2018) 154–160, https://doi.org/10.1016/j.scriptamat.2017.06.041.
[59] C. Heintze, F. Bergner, R. Kögler, R. Lindau, The influence of helium and ODS on the irradiation-induced hardening of Eurofer97 at 300°C, Adv. Sci. Technol. 73 (2010) 124–129, https://doi.org/10.4028/www.scientific.net/AST.73.124.
[60] A. Hardouin Duparc, C. Moingeon, N. Smetniansky-de-Grande, A. Barbu, Microstructure modelling of ferritic alloys under high flux 1 MeV electron irradiations, J. Nucl. Mater. 302 (2002) 143–155, https://doi.org/10.1016/S0022-3115(02)00776-6.
[61] B. Duan, C. Heintze, F. Bergner, A. Ulbricht, S. Akhmadaliev, E. Oñorbe, Y. de Carlan, T. Wang, The effect of the initial microstructure in terms of sink strength on the ion-irradiation-induced hardening of ODS alloys studied by nanoindentation, J. Nucl. Mater. (2017), https://doi.org/10.1016/j.jnucmat.2017.08.014.
[62] J.C. Haley, S. de Moraes Shubeita, P. Wady, A.J. London, G.R. Odette, S. Lozano-Perez, S.G. Roberts, Microstructural examination of neutron, proton and self-ion irradiation damage in a model Fe9Cr alloy, J. Nucl. Mater. 533 (2020) 152130, , https://doi.org/10.1016/j.jnucmat.2020.152130.
[63] M. Butterling, F. Bergner, C. Heintze, W. Anwand, A. Ulbricht, Application of positron annihilation spectroscopy to the study of irradiated Fe-Cr alloys, Defect Diffus. Forum. 331 (2012) 165–179, https://doi.org/10.4028/www.scientific.net/DDF.331.165.
[64] G.S. Was, Challenges to the use of ion irradiation for emulating reactor irradiation, J. Mater. Res. 30 (2015) 1158–1182, https://doi.org/10.1557/jmr.2015.73.
[65] G. Bonny, D. Terentyev, L. Malerba, New contribution to the thermodynamics of Fe-Cr Alloys as base for ferritic steels, J. Phase Equilibria Diffus. 31 (2010) 439–444, https://doi.org/10.1007/s11669-010-9782-9.
[66] M.J. Swenson, J.P. Wharry, Nanocluster irradiation evolution in Fe-9%Cr ODS and ferritic-martensitic alloys, J. Nucl. Mater. 496 (2017) 24–40, https://doi.org/10.1016/j.jnucmat.2017.08.045.
[67] M.J. Swenson, J.P. Wharry, TEM characterization of irradiated microstructure of Fe-9%Cr ODS and ferritic-martensitic alloys, J. Nucl. Mater. 502 (2018) 30–41, https://doi.org/10.1016/j.jnucmat.2018.01.062.
[68] M. Lambrecht, L. Malerba, Positron annihilation spectroscopy on binary Fe–Cr alloys and ferritic/martensitic steels after neutron irradiation, Acta Mater. 59 (2011) 6547–6555, https://doi.org/10.1016/j.actamat.2011.06.046.